Ocean Engineering 328 (2025) 121031

Contents lists available at ScienceDirect

Ocean Engineering

journal homepage: www.elsevier.com/locate/oceaneng

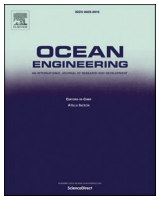

Research paper

Design and experimental tests for novel shapes of floating OWC wave energy converters with the additional purpose of breakwater

Xiangcheng Lyu [a], Chenhao Mi [a], Stan Collions [a], Wenchuang Chen [b,*], Danlei Yang [a,**], Luofeng Huang [a]

[a] Faculty of Engineering and Applied Sciences, Cranfield University, Cranfield, MK43 0AL, United Kingdom
[b] School of Civil Engineering, Sun Yat-Sen University, Zhuhai, 519082, China

ARTICLE INFO

Keywords:
Renewable energy
Wave energy converter
Oscillating water column
Experiments
Capture width ratio

ABSTRACT

The oscillating water column (OWC) is a type of wave energy converter (WEC) that captures the energy of incoming waves. As waves reach the structure, their movement causes the water within an enclosed chamber to oscillate, creating airflow that powers a turbine, generating electricity. This principle can be applied to the design of breakwaters, which can protect marine structures such as floating solar farms and wind turbines. This study involved designing two types of buoyancy chambers for the OWC-WEC and two underneath baffles with adjustable spacing. These configurations were tested in a wave tank to assess wave energy capture, wave attenuation, hydrodynamics, and mooring forces. The experimental results demonstrate that a baffle spacing of 1 m, combined with a V-type buoyancy chamber, significantly enhances the wave energy capture and wave attenuation performance of the OWC. This configuration achieves up to a 57.09 % increase in the capture width ratio and a maximum reduction of 20.88 % in the wave transmission coefficient. Furthermore, mooring line forces are reduced by 21.86 %, while the baffles effectively mitigate pitch motion. Notably, greater pitch reduction improves the capture width ratio. In conclusion, this study introduces a novel wave energy converter, providing key insights for future marine energy development.

1. Introduction

Ocean energy technologies could generate more than twice the electricity currently needed worldwide (IRENA, 2020) (Tumse et al., 2024). Moreover, they offer the potential to supply reliable and predictable power to coastal nations and small island developing states. Considering that around 40 % of the global population—approximately 3 billion people—resides within 100 km of the coast, and that small island developing states have a combined population of around 65 to 70 million, advancing ocean energy technologies is essential for fostering the development of the blue economy (IRENA, 2023a) (IRENA, 2023b).

Among the various marine renewable energy options, wave energy stands out for its abundant reserves. However, wave energy technologies are still not fully mature and face challenges such as high costs and harsh marine environments (Pecher and Kofoed, 2017). To enhance energy efficiency and distribute the construction costs of infrastructure, integrating multiple marine energy sources and various offshore structures has become a trend, such as solar energy – wave energy integrations, wind energy – wave energy integration (Solomin et al., 2021) and wave energy – breakwater integrations (Mustapa et al., 2017). These strategies can harness the distinct advantages of various marine energy sources, facilitate the shared use of infrastructure and space, and advance wave energy industrialisation (Zhao et al., 2019).

In marine engineering, breakwaters are frequently implemented to safeguard infrastructure (McCartney, 1985). Breakwaters and wave energy converters are often deployed under similar oceanic environmental conditions, and they also share some similarities in their structural design. As these two types of structures can be integrated, numerous breakwater–wave energy converter systems have been proposed, such as the hybrid WEC-breakwater system combining an oscillating water column and an oscillating buoy (Cheng et al., 2022), a pile-restrained floating breakwater-the oscillating buoy (OB) type (Ning et al., 2016) (Chen et al., 2024a), a pile-supported OWC-type structure as breakwaters (He and Huang, 2014) and a sketch of the floating skirt

* Corresponding author.
** Corresponding author.
E-mail addresses: chenwch37@mail.sysu.edu.cn (W. Chen), danlei.yang@cranfield.ac.uk (D. Yang).

https://doi.org/10.1016/j.oceaneng.2025.121031
Received 13 January 2025; Received in revised form 13 March 2025; Accepted 18 March 2025
Available online 24 March 2025

breakwater with OWC (Sundar, 2010) (Wang et al., 2024). The motivation for investigating this specific system stems from the rising demand for multifunctional offshore structures. The proposed floating OWC-WEC system is designed not only to function as a wave energy harvester but also to serve as a floating breakwater, providing protection for various offshore structures, such as floating solar farms. Unlike conventional breakwaters that solely mitigate wave transmission, this hybrid structure simultaneously reduces wave impact while converting wave energy into electricity, enhancing offshore renewable energy generation and improving structural stability (Mustapa et al., 2017).

Among them, oscillating water column wave energy converters (OWC-WECs) have been proven to be an effective way of wave energy extraction. A wave energy converter (WEC) is a device that captures the movement, pressure variations, and water level changes generated by ocean waves, converting them into electricity (de and Falcão, 2010). WECs offer considerable potential, particularly in areas with long coastlines and abundant wave energy resources (Khurshid et al., 2024). The oscillating water column (OWC) is a type of wave energy converter that is valued for its simplicity and cost-effectiveness. Its design ensures that the primary moving parts do not come into direct contact with seawater, enhancing durability (Delmonte et al., 2016). The energy conversion process in an OWC involves three main stages (de and Falcão, 2010). The movement of waves causes the water column within the chamber to oscillate, which in turn drives the air in the chamber to move, converting wave energy into pneumatic energy. The compressed air is then channelled through a duct, driving a unidirectional air turbine, thus converting pneumatic energy into mechanical energy. Finally, the mechanical energy from the turbine is converted into electricity via a generator (Qiao et al., 2020). The OWC can be categorised into fixed and floating types. Among them, the backward bent duct buoy (BBDB), as a representative of floating OWC devices, has demonstrated outstanding performance (Chen et al., 2024b). BBDB was developed to direct waves through an L-shaped channel, resulting in nearly total reflection (Masuda and Mccormick, 1987), as shown in Fig. 1. The BBDB is an OWC wave energy converter with high primary conversion efficiency and low mooring costs (Toyota et al., 2008).

Rectangular-section breakwaters, which can also be classified as fixed or floating, are frequently deployed due to their simplicity and durability. Floating breakwaters (FBs) offer greater flexibility and adaptability to variations in water levels and wave conditions compared to their bottom-fixed counterparts (Widagdo et al., 2020). The performance of floating breakwaters is significantly affected by the ratio of length to wavelength and draft to water depth. Adjusting these geometric parameters can substantially improve their ability to dissipate wave energy (Cebada-Relea et al., 2022). A pontoon breakwater can achieve significant performance improvements by incorporating air chambers and additional plates into its structure. Integrating a pneumatic damping system into the breakwater allows for effective regulation of airflow velocity at the chamber outlet, thereby enhancing wave energy absorption. Simultaneously, the addition of plates not only improves structural stability but also optimises overall functionality.

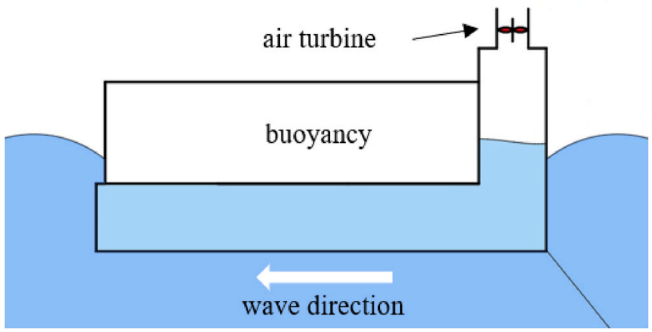

Fig. 1. The structure of the backward bent duct buoy (BBDB).

Studies have demonstrated that pontoons equipped with such a system can achieve efficiency gains of up to 20 % (Koo, 2009) (Mao et al., 2024).

In past studies, the approaches employed to study the interaction between waves and WECs encompassed theoretical, numerical, and experimental methods. Theoretical analyses are commonly performed based on linear potential flow theory, often applying the matching eigenfunction method (Göteman, 2017). The evaluation of OWC devices through two-dimensional computational fluid dynamics (CFD) simulations indicates that the hydrodynamic performance of the converter is influenced not only by its design but also by its interaction with the surrounding marine environment (Mia et al., 2022). The cylindrical OWC's nonlinear behaviour revealed that the water column formation phenomenon is associated with the second-order nonlinear components of the incident waves (Zhang et al., 2023). The mooring system plays a critical role in ensuring the operational efficiency and stability of these converters (Kisacik et al., 2020a). Different orifice sizes were used to represent various power take-off (PTO) damping levels, analysing the hydrodynamic and aerodynamic performance of OWCs. A quadratic nonlinear relationship was observed between orifice pressure and airflow rate, like the behaviour in impulse turbines (Sheng et al., 2012). Some studies aim to enhance energy conversion efficiency by harnessing the reflected energy of breakwaters (Howe and Nader, 2017).

Due to the structural and functional similarities between BBDB-WECs and pontoon-type breakwaters, particularly the damping effect of the gas, this study integrates their features to develop a novel wave energy converter functioning as a breakwater. The proposed device features a BBDB equipped with baffle structures and an adjustable buoyancy chamber. The research explores the effects of varying baffle spacing and different wave energy converter configurations on wave energy capture performance, wave attenuation efficiency, and mooring forces. Additionally, this study examines the relationship between these performance metrics and the motion of the wave energy converter. Systematic experiments and data analysis were conducted, and the findings provide valuable design insights for the integration of WECs with breakwater structures.

This manuscript is organised as follows. The methodology is developed in section 2, including section 2.1 for the geometry of the prototype, section 2.2 for the experimental environment, section 2.3 for the sensor, and section 2.4 for the experimental procedure. The data analysis is developed in section 3, including section 3.1 for capture width ratio, section 3.2 for transmission coefficient, and section 3.3 for load on mooring lines. The experimental results are presented and discussed in section 4. Section 5 summarises this research and provides recommendations for future work.

2. Methodology

2.1. Physical model

In this study, the OWC-WEC model is developed based on the bent duct buoy (BDB), which is a floating system without relative moving parts, ensuring high reliability and survivability. Depending on the direction of wave incidence, the structure can be categorised as either a backward bent duct buoy (BBDB) or a forward bent duct buoy (FBDB). Two distinct shapes of buoyancy chambers, A-type buoyancy chamber and V-type buoyancy chamber are shown in Fig. 2. Inspired by pontoon floating breakwaters, a novel baffle system was installed beneath the model. The experiment investigates the impact of various factors, including wave direction (BBDB and FBDB), buoyancy chamber shape, the presence or absence of baffles, and different baffle spacings, on the overall performance.

This study compares A-type and V-type buoyancy chambers to optimise energy capture and wave attenuation performance in the OWC-WEC structure. The A-type buoyancy chamber features a ship-like design, with its straight sidewalls minimising interference from

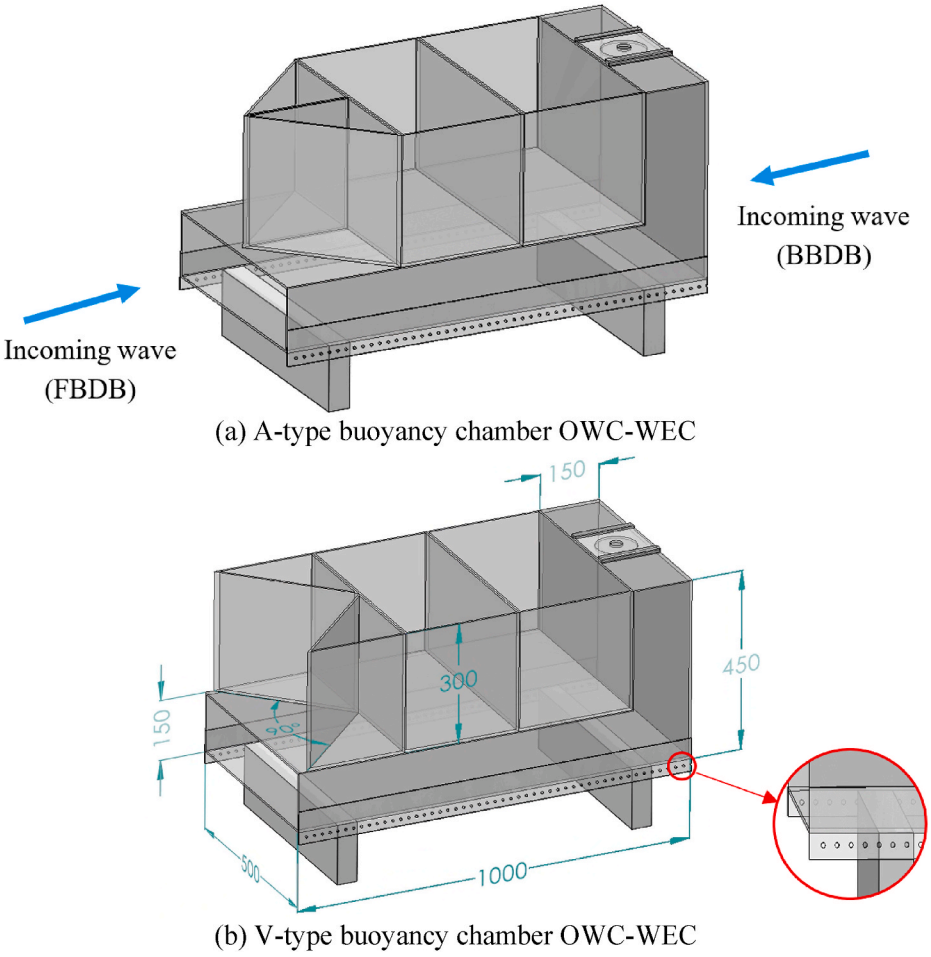

Fig. 2. Model of the OWC-WEC.

incident waves, providing a more stable hydrodynamic environment, and enhancing the consistency of wave energy conversion. In contrast, the V-type buoyancy chamber creates an energy collection region, which may result in a greater motion response.

An orifice nozzle simulates the damping effect typically provided by an air turbine. The radius of the nozzle, r_0, determines the level of damping: if r_0 is too large, the pressure differential between the air chamber and the external atmosphere approaches zero. Conversely, if r_0 is too small, airflow through the nozzle becomes negligible. In both extreme conditions, the energy captured by the device would be zero (Kisacik et al., 2020b). Therefore, achieving the optimal capture width ratio (CWR) requires determining the ideal nozzle ratio ζ (the ratio of the nozzle area to the air chamber cross-sectional area). To facilitate this, interchangeable nozzles with proper sealing were used to prevent air leakage, which could otherwise skew the experimental results. The nozzle diameters are detailed in the following Table 1.

To simplify the reconfiguration of the model, all components except the main bent duct, including the buoyancy chambers and baffles, are designed for easy replacement and are secured with bolts. The lower part of the model features a perforated plate, which connects the baffles to the anchoring system. The holes in the plate are spaced 20 mm apart, allowing for precise adjustment of the baffle spacing, as shown in Fig. 2.

Table 1
Nozzle diameters and nozzle ratio.

Nozzle Diameter	30 mm	35 mm	40 mm	45 mm
Nozzle Ratio	1.03 %	1.40 %	1.83 %	2.32 %

To enable clear observation of the water column oscillations within the air chamber, the model is constructed using 5 mm thick acrylic sheets with a density of 1190 kg·m^{-3}, while the perforated plate is made from 3 mm thick acrylic, assembled with Tensol-70 (acrylic cement) adhesive. The baffles are crafted from Styrofoam with a density of 38.44 kg·m^{-3}. Precision during assembly is essential to ensure the model remains airtight. A transparent PE film is applied over the model to prevent water from splashing into the buoyancy chambers during experiments, which could otherwise affect buoyancy and draft depth. This design follows the geometric and physical parameter optimisations for the BBDB-OWC (Wu et al., 2017) (Chen et al., 2017) (Li et al., 2019), where the inlet size influences the airflow characteristics within the chamber and the energy conversion efficiency, as an excessively large opening reduces air pressure and affects turbine performance, while an overly small opening may restrict water inflow and limit wave energy

Table 2
Parameters of the physical model.

Parameter	Unit	Value
Model Length L	m	1.000
Model Width b	m	0.500
Model Height h	m	0.450
Draught h_{dr}	m	0.219
Inlet Height h_{in}	m	0.150
Air Chamber Length l_a	m	0.150
Buoyancy Chamber Length l_b	m	0.867
Nozzle Radius r_0	m	0.03–0.045
Nozzle Ratio ζ	m	1.03–2.32
Baffle Spacing l_s	m	0.2–1

conversion. The specific physical parameters of the BBDB-OWC model used in this study are listed in Table 2. The model weighs 21.5 kg, and additional weights were added during the experiment to reach the designed waterline. The displacement in the laboratory tests was 25.7 kg.

Due to the constraints of the experimental environment, the model was scaled down to fit within the wave tank. To ensure that the experimental conditions accurately reflect those of a natural ocean environment, it is crucial to choose an appropriate scale to minimise the impact of wave reflections from the tank walls. The model must maintain similarity to the full-scale prototype by satisfying three essential criteria: geometric, kinematic, and dynamic similarities. The wave parameters within the tank should also adhere to these principles. In this context, where inertial forces outweigh viscous forces, the Froude number is more relevant than the Reynolds number. Maintaining a constant Froude number (as shown in Eq. (1)) throughout the scaling process is vital for preserving kinematic and dynamic similarity (Windt et al., 2021).

$$\text{Froude number (Fr)} = \frac{U_p}{\sqrt{gL_p}} = \frac{U_m}{\sqrt{gL_m}} \tag{1}$$

where U is the fluid velocity [m/s], where T is the period [m] and L is the characteristic length [m].

Table 3 outlines the scaling ratios used in this study, based on the guidelines for applying Froude scaling in wave tank experiments.

2.2. Experimental set-up

The experiments were conducted in the Ocean wave tank at Cranfield University. The length of the wave tank is $l_t = 30$ m, the width of the wave tank is $l_t = 1.5$ m, and it was filled with fresh water of 1.5 m. An artificial beach, constructed from curved steel plates, was installed to absorb wave energy and reduce reflective waves. This wave tank has the capability to generate wave heights ranging from 0.005 m to 0.28 m, with wave frequencies from 0.1 Hz to 1.1 Hz. In the present experiment, the still water depth is set to be $d = 1.5$ m. There is almost no reflection at the wave maker. The beach attenuates incident waves. The layouts of the model and sensors are shown in Fig. 3.

2.2.1. Mooring system

The design methodology of the mooring system for the floating structure follows relevant certification standards and considers three critical limit states: the Ultimate Limit State (ULS), the Accidental Limit State (ALS), and the Fatigue Limit State (FLS) (Vryhof Anchors, 2015) (see Fig. 4). In this study, the mooring system is composed of four pre-tensioned polyester ropes, each with a diameter of 0.5 mm and a stiffness coefficient of 4620 N/m.The spring stiffness is 130.66 N/m. One end of each rope is attached to a perforated plate beneath the OWC-WEC model, while the other end is secured to 10 kg counterweights located at the four corners of the wave tank. Pulleys are incorporated with the counterweights to redirect the force without altering its magnitude, allowing tension sensors to be mounted on aluminium bars above the wave tank. This setup prevents the sensors from coming into direct contact with the water and minimises errors caused by sensor movement in tandem with the model, as shown in Fig. 3.

Table 3
Froude scaling summary for model and prototype.

Quantity	Prototype-model ratio	Scale relationship	Scale factor
Linear Dimensions	L_P/L_m	S	10
Linear Velocity	V_P/V_m	$S^{1/2}$	$10^{1/2} = 3.162$
Acceleration	a_P/a_m	1	1
Area	A_P/A_m	S^2	$10^2 = 100$
Volume	∇_P/∇_m	S^3	$10^3 = 1000$
Angle	α_P/α_m	1	1
Angular Velocity	$\dot{\alpha}_P/\dot{\alpha}_m$	$S^{-1/2}$	$10^{-1/2} = 0.316$
Wave Height	H_P/H_m	S	10
Wave Length	λ_P/λ_m	S	10
Wave Period	T_P/T_m	$S^{1/2}$	$10^{1/2} = 3.162$
Wave Frequency	f_P/f_m	$S^{-1/2}$	$10^{-1/2} = 0.316$
Mass	m_P/m_m	γS^3	$1.025 \times 10^3 = 1025$
Force	F_P/F_m	γS^3	$1.025 \times 10^3 = 1025$
Power	P_P/P_m	$\gamma S^{7/2}$	$1.025 \times 10^{7/2} = 3241.33$

2.2.2. Wave parameters

Previous studies have shown that the energy capture efficiency of OWC-WEC devices is particularly sensitive to variations in wave frequency. The range of frequency response is crucial to the device's operational efficiency and longevity, while wave height primarily serves to enhance performance within the working frequency band. Given the significance of device performance across different frequencies (or wavelengths), this aspect has remained a central focus in OWC-WEC studies (Endre Süli and David Francis Mayers, 2003a). Therefore, this experiment utilises a fixed wave height to compare performance across various frequencies. It is important to acknowledge that while this study uses regular waves with controlled incidence, real sea states exhibit directional irregularities that impact energy conversion efficiency. Future research should extend this study by incorporating numerical simulations that consider multi-directional wave spectra. Recent studies have provided fully spectral approaches that allow for a more accurate representation of real sea states, which could further refine the performance assessment of the proposed system (Adibzade and Akbari, 2023) (Adibzade and Akbari, 2024).

The wavelength can be determined based on the dispersion relation derived from linear wave theory (Wehausen et al., 1960), as expressed by:

$$\frac{2\pi}{\lambda}\tanh\left(\frac{2\pi h}{\lambda}\right) = \frac{\omega^2}{g} \tag{2}$$

Where λ denotes the wavelength, $g = 9.81\text{m/s}^2$ represents the acceleration due to gravity, $\omega = 2\pi f$ is the angular frequency. The wave parameters used in the experiment are detailed in Table 4.

2.2.3. Sensors

The study used nine sensors: four wave gauges, two pressure sensors, two force sensors, and one accelerometer-inclinometer, as shown in Fig. 5. The pressure sensor is PMP 4170, with an accuracy of ± 0.04 %. The measurement range of the sensors is −100mbar to +100 mbar. The sensor operates at a sampling frequency of 50 Hz. The weight of the sensor is 200 g Utilising two sensors enhances data accuracy by allowing the identification and exclusion of outlier data points. To ensure the precision and reliability of measurements, both sensors underwent rigorous calibration prior to the experiments.

The accelerometer-inclinometer is WT901C, with an accuracy of 0.05 for static measurements and 0.1 for dynamic measurements. It has an angle range of ± 180° for the X and Z axes and ± 90° for the Y axis. The sensor operates at a sampling frequency of 50 Hz. The accelerometer-inclinometer is used to measure the motion of the model and orientation within an orthogonal plane. It records rotational angles and translational accelerations in three directions. These devices are positioned along the model's centreline, aligned with the centreline of the wave tank, with the positive X-axis pointing towards the wave generator.

One wave gauge was positioned upstream and another downstream along the centreline to monitor changes and calibrate wave height before and after the model. Inside the air chamber, two wave gauges were installed to capture the complex fluctuations of the liquid surface,

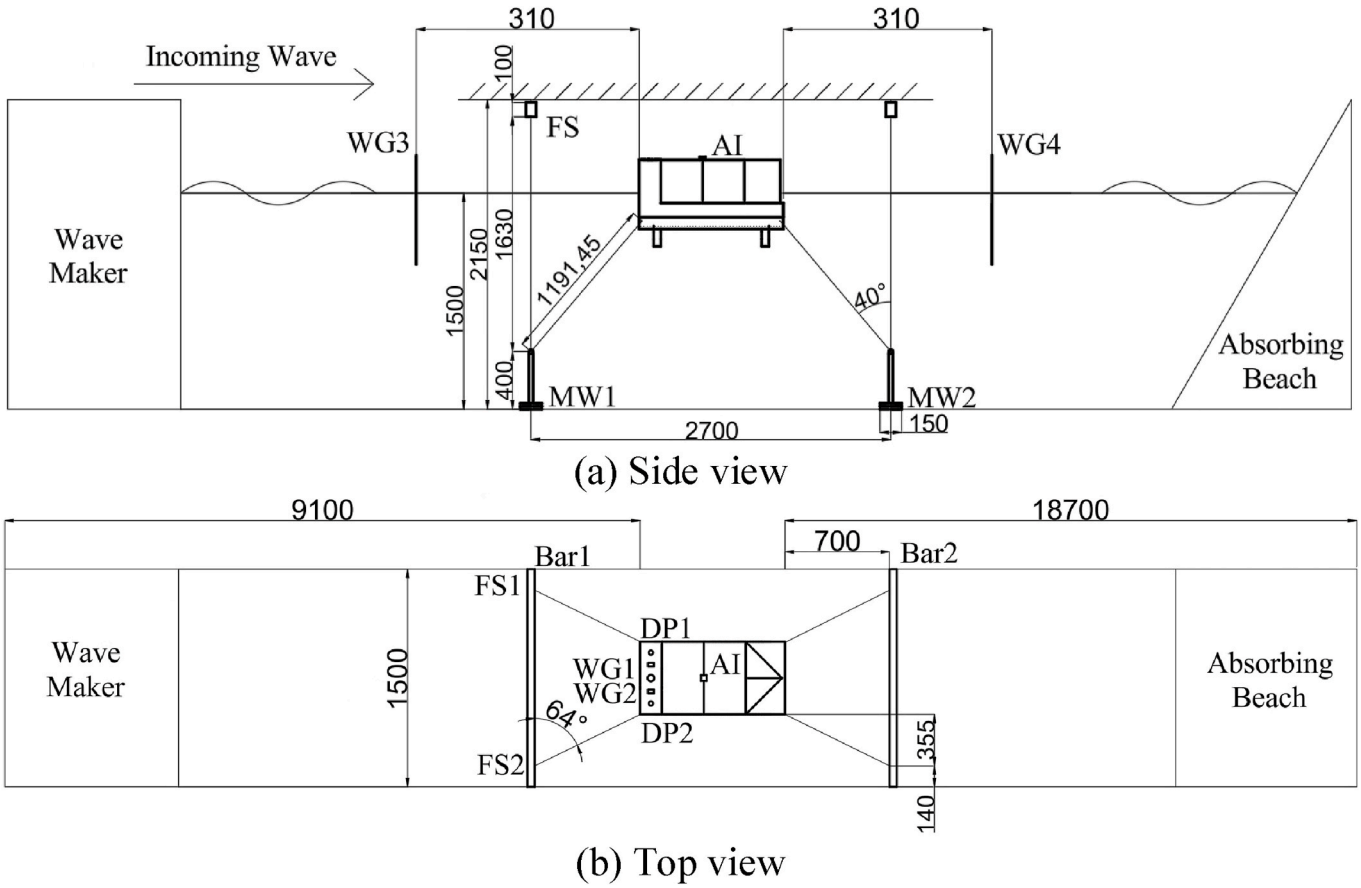

Fig. 3. Experimental setup.

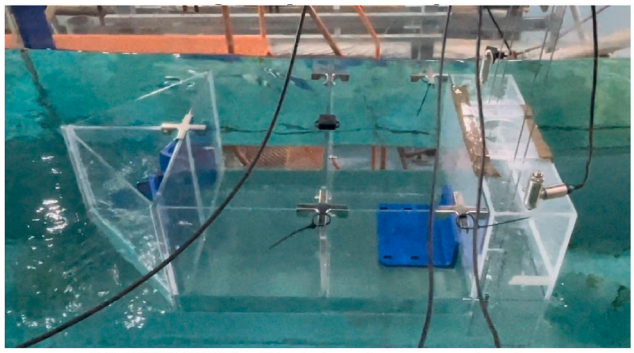

(a) OWC-WEC with A-type buoyancy chamber

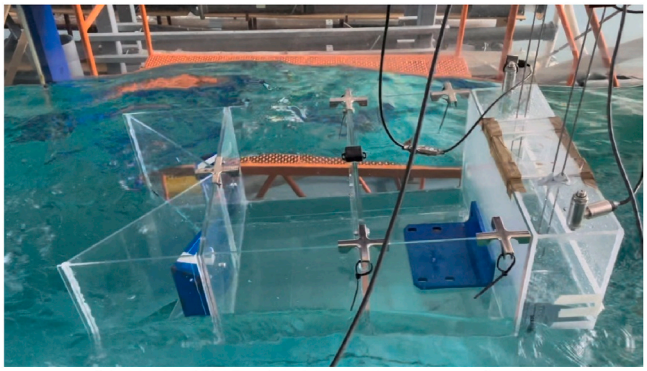

(b) OWC-WEC with V-type buoyancy chamber

Fig. 4. OWC-WEC placement in the water tank.

Table 4
Wave parameters of experiment and real-world scenarios.

	Experimental Values			Real-World Values		
	H[m]	λ/m	f/Hz	H[m]	λ/m	f/Hz
1	0.1	9.75	0.4	1	97.5	0.126
2	0.1	6.24	0.5	1	62.4	0.158
3	0.1	4.33	0.6	1	43.3	0.190
4	0.1	3.18	0.7	1	31.8	0.221
5	0.1	2.44	0.8	1	24.4	0.253
6	0.1	1.93	0.9	1	19.3	0.285
7	0.1	1.56	1.0	1	15.6	0.316
8	0.1	1.29	1.1	1	12.9	0.348
9	0.1	1.08	1.2	1	10.8	0.379

enabling detailed hydrodynamic analysis. All wave gauges are capacitive gauges These sensors have a measurement range of 0 m ~1 m and an accuracy of 0.2 %. The sensor operates at a sampling frequency of 50 Hz. Before deployment, each wave gauge was subjected to a rigorous calibration process.

The force sensor used is Go Direct Force and Acceleration Sensor, with a measurement accuracy of 0.1 N, a range of ± 90N, and a sampling frequency of 50 Hz. The sensors and springs are designed to measure the load on the mooring lines. Springs attached to the sensor hooks provide both damping and suspension, resulting in load variation waveforms that are more straightforward to analyse. To ensure precise data collection, two of these sensors were strategically placed at the front of the model.

2.3. Experimental procedure

To minimise random experimental errors, each test was conducted at

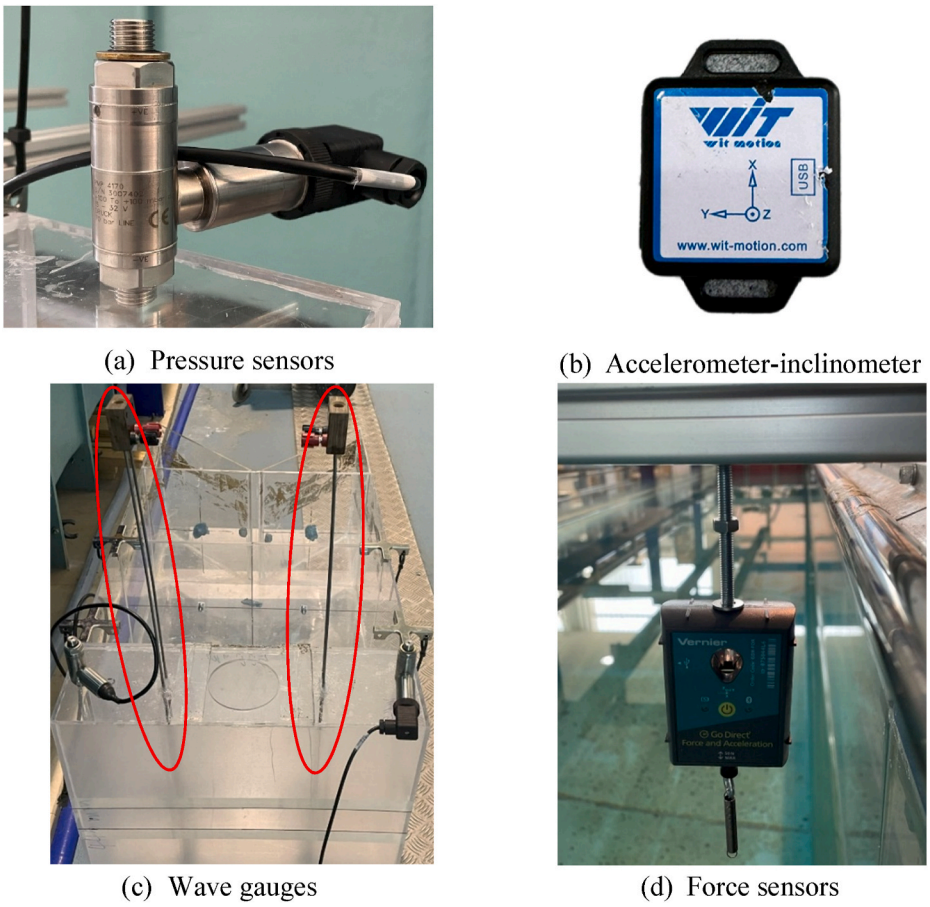

(a) Pressure sensors (b) Accelerometer-inclinometer

(c) Wave gauges (d) Force sensors

Fig. 5. Photos of the sensors applied in the experimental study.

least three times. The coefficient of variation was calculated in real time for each set of measurements. Outliers were excluded, and the tests were repeated until the coefficient of variation was below 3 % . Each experiment lasted approximately 15 wave periods, during which the system response curve reached a stable state. To begin, wave parameters were calibrated without the model to ensure that the experiments would be conducted at precise wave heights and frequencies (Chen et al., 2021).

To streamline the experimental process, the first step was to determine the optimal nozzle ratio for the OWC-WEC model. Although the optimal ratio varies depending on the structure, it typically ranges from 0.9 % to 2 %.

After determining the optimal nozzle ratio, the study explored the impact of different buoyancy chamber shapes (V-type and A-type) and varying wave incidence directions (BBDB and FBDB) on model performance. Based on the experimental outcomes, the two most effective configurations without baffles were selected for further investigation, focusing on the influence of baffles.

Finally, the study examined the effects of baffle installation and different baffle spacings on performance, testing five spacing intervals (1 m, 0.8 m, 0.6 m, 0.4 m, and 0.2 m), as shown in Fig. 6. In line with real-world considerations for energy efficiency and cost-effectiveness, the authors prioritise the power generation capabilities of the OWC-WEC over its wave attenuation performance.

3. Data analysis

3.1. Capture width ratio

The capture width ratio (CWR) is a key indicator of the WEC efficiency. It quantifies the proportion of wave energy captured by the device relative to the energy available across the width of its wave-facing side, as defined by Eq. (5). Essentially, CWR reflects the performance of the first stage of energy conversion in an OWC system.

The first step in determining the CWR is to estimate the energy captured by the device, which depends on measuring the airflow into and out of the air chamber. Direct airflow measurement using a flow meter introduces additional damping, which may alter the device's dynamic response. Therefore, an indirect measurement approach is adopted to simulate the effects of an air turbine.

The movement of airflow in and out of the chamber is driven by changes in the water surface level. Two alternative approaches can be used to estimate these airflow variations:

- **Wave gauges:** Wave gauges monitor the wave height within the chamber. The variations in the water column volume observed through these measurements are used to infer the corresponding changes in air volume.
- **Pressure sensors:** Pressure sensors are used to detect fluctuations in chamber pressure. By applying the flow-pressure relationship, the resulting airflow can be calculated.

However, during experiments, the water surface inside the chamber often becomes unstable, with sloshing and splashing effects becoming more pronounced at higher wave frequencies. This dynamic behaviour complicates the use of wave gauges for accurately tracking changes in water column volume. Additionally, air compressibility may not be fully accounted for, further limiting the accuracy of this method. The calculation process is illustrated in Eqs. (3)–(6) (Sheng et al., 2012) (He and Huang, 2017) (Zhu et al., 2024).

The instantaneous airflow rate $Q(t)$ is calculated using the flow rate-

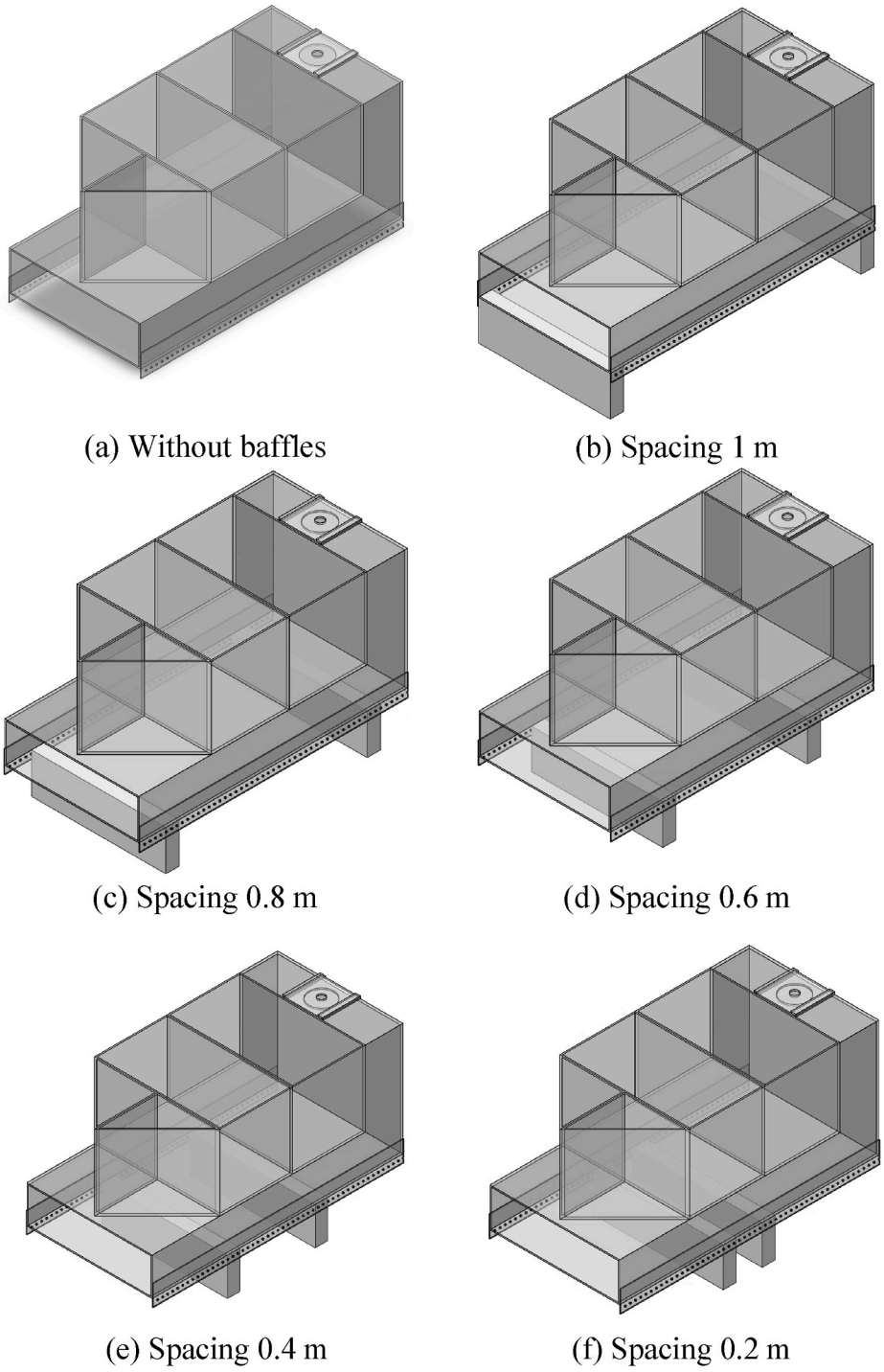

Fig. 6. Six OWC-WEC configurations.

pressure relationship as follows:

$$Q(t) = C_q \pi r_0^2 \sqrt{\frac{2|p(t)|}{\rho_a}} \tag{3}$$

Where C_q is the flow coefficient, which, based on reference (Sheng et al., 2012), is taken as 0.65 for the floating OWC device's air chamber, r_0 is the orifice nozzle radius, as defined earlier. ρ_a is the air density.

The following Eq. (4) describes the average energy captured by the device:

$$P = \frac{1}{T}\int_0^T p(t)Q(t)dt \tag{4}$$

The average energy per unit width of the incident wave over one cycle, derived from potential flow theory, is given by the following formula:

$$P_{in} = \frac{\rho g H^2}{8}\frac{\omega}{2k}\left[1 + \frac{2kh_d}{\sinh(2kh_d)}\right] \tag{5}$$

Where ρ is the water density, g is the acceleration due to gravity, H is the wave height, ω is wave angular frequency, k is the wave number, h_w is

the water depth.

The CWR of the device is:

$$\mathrm{CWR} = \frac{P}{P_{in} b} \times 100\% \tag{6}$$

3.2. Wave transmission coefficient

When waves encounter a marine structure, part of the energy is dissipated through processes like diffraction, reflection, refraction, and scattering, while the remaining energy that passes through the structure is quantified by the wave transmission coefficient (K_t).

K_t is the ratio of the transmitted wave amplitude to the incident wave amplitude. A_t is obtained by performing a Fast Fourier Transform (FFT) on the wave data collected by the wave gauge located downstream, expressed by the following formula:

$$K_t = \frac{A_t}{A_i} \tag{7}$$

Where A_t and A_i are amplitudes of transmitted and incident waves respectively.

This coefficient is essential for optimising the design of such structures, as it provides insight into how effectively the structure reduces the transmission of wave energy.

3.3. Load on mooring lines

The effectiveness of the mooring system's restraint is determined by measuring the tension in the mooring lines. Since the forces acting on each mooring line as a result of the model's motion are not uniform, two sensors are used to calculate the average load. The raw data collected by the force sensors can be analysed in the time domain to help understand the instantaneous behaviour of the OWC-WEC model. Furthermore, the FFT was performed to convert the time domain data into the frequency domain, providing insights into the distribution of wave energy across different frequencies. Frequency domain analysis is particularly useful for studying the response of the system to periodic waves or in steady-state conditions (Uddin et al., 2019) (Mani, 1991) (Endre Süli and David Francis Mayers, 2003b).

3.4. Model motion

In wave tank experiments, the OWC-WEC device has six degrees of freedom (DoFs). For the purposes of this study, the analysis is simplified by focusing on three key motion types: heave motion (A_s), surge motion (A_h), and pitch motion (Θ_p). To make the resulting motion values dimensionless, the concept of the response amplitude operator (RAO) is utilised. It is defined as the ratio of the motion amplitude of the model to the inciting amplitudes within the incident wave. The RAOs for surge, heave, and pitch motions are formulated as shown in Eqs. (8)–(10) (Huang and Thomas, 2019):

$$\mathrm{RAO}_{\mathrm{surge}} = \frac{A_s}{A_i \cosh(kd)} \tag{8}$$

$$\mathrm{RAO}_{\mathrm{heave}} = \frac{A_h}{A_i} \tag{9}$$

$$\mathrm{RAO}_{\mathrm{pitch}} = \frac{\Theta_p}{kA_i} \tag{10}$$

Where k is wave number, d denotes the still water depth as defined, A_i denotes the wave amplitude, Θ_p denotes the motion angles.

4. Results and discussion

4.1. Effect of nozzle ratios

Fig. 7 illustrates the variation in the CWR with different nozzle ratios for the A-type buoyancy chamber BBDB-WEC without baffles. Among the four nozzle diameters tested, CWR shows a clear pattern in relation to the nozzle ratio. From $\lambda/L = 1.08$ to $\lambda/L = 6.24$, CWR increases as the nozzle ratio decreases, with the 30 mm diameter nozzle ($\zeta = 1.03$ %) delivering the best performance. However, at $\lambda/L = 9.75$, the trend reverses, with larger nozzles yielding higher CWR, increasing from 10.07 % to 17.64 %. It should be a gradual rise in CWR, as shown in Fig. 9, between $\lambda/L = 1.08$ and $\lambda/L = 2.44$, followed by a steady decline from $\lambda/L = 2.44$ to $\lambda/L = 9.75$. Notably, at $\lambda/L = 2.44$, represents the point where all four diameters achieve their maximum CWR values. For D = 30 mm, it should be 124.18 % as the peak value, significantly higher than the corresponding peak values for the other diameters. Additionally, the average CWR within the examined λ/L exhibits the highest value for D = 30 mm, approximately 48.07 %, which is 5.23 % higher than that for D = 40 mm, which has the lowest average CWR, around 42.84 %. The nozzle ratio for the subsequent experiments is 1.03 % (D = 30 mm).

4.2. Comparison of different model configurations

4.2.1. CWR performance

Fig. 8 compares the CWR of four different buoyancy chamber configurations: A-type buoyancy chamber BBDB, V-type buoyancy chamber BBDB, A-type buoyancy chamber FBDB, and V-type buoyancy chamber FBDB, over a range of normalised wavelengths (λ/L). The A-type buoyancy chamber BBDB achieves the highest peak efficiency at $\lambda/L = 2.44$, reaching 124.18 %, followed by the V-type buoyancy chamber BBDB at 116.55 %. The FBDB configurations show lower overall performance, with peaks below 40 %. Beyond $\lambda/L = 4.33$, all designs converge to similarly low values. The average CWR values across the entire range of λ/L are 48.07 % for A-type buoyancy chamber BBDB, 49.05 % for V-type buoyancy chamber BBDB, 9.57 % for A-type buoyancy chamber FBDB, and 15.74 % for V-type buoyancy chamber FBDB. Overall, The V-type buoyancy chamber BBDB demonstrates the best energy capture efficiency, particularly in the peak region.

In summary, BBDB-WEC configurations demonstrate superior wave energy capture capabilities compared to FBDB-WEC. Additionally, the V-type buoyancy chamber exhibits stronger performance at lower λ/L.

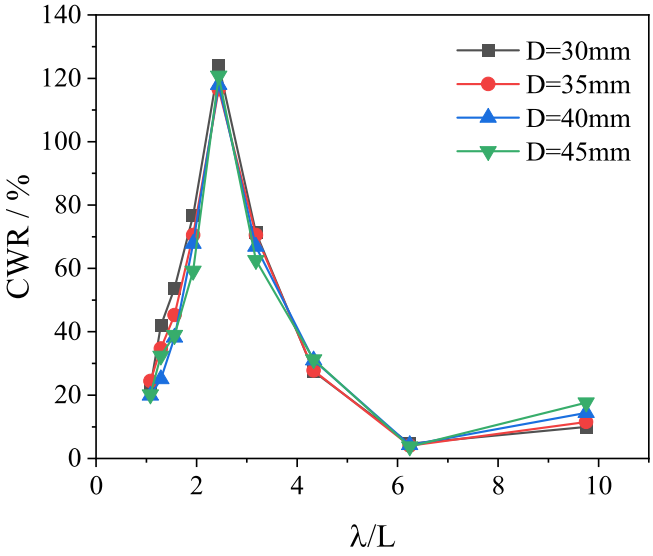

Fig. 7. Variation of CWR with λ/L under different nozzle ratios.

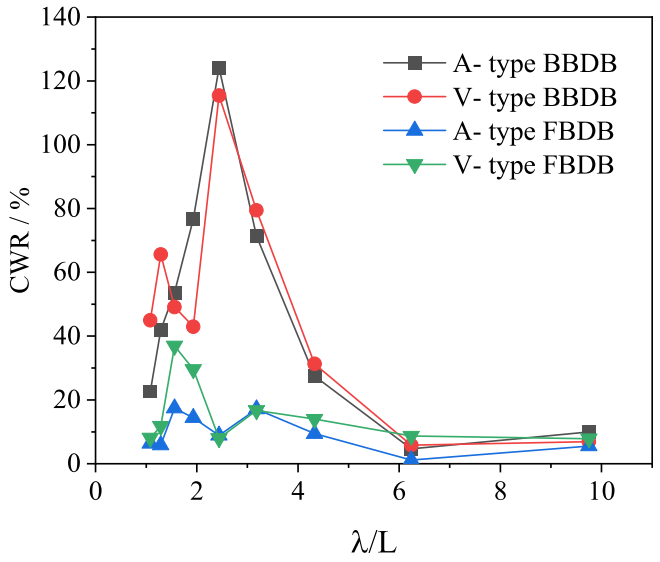

Fig. 8. Variation of CWR with λ/L under four different configurations.

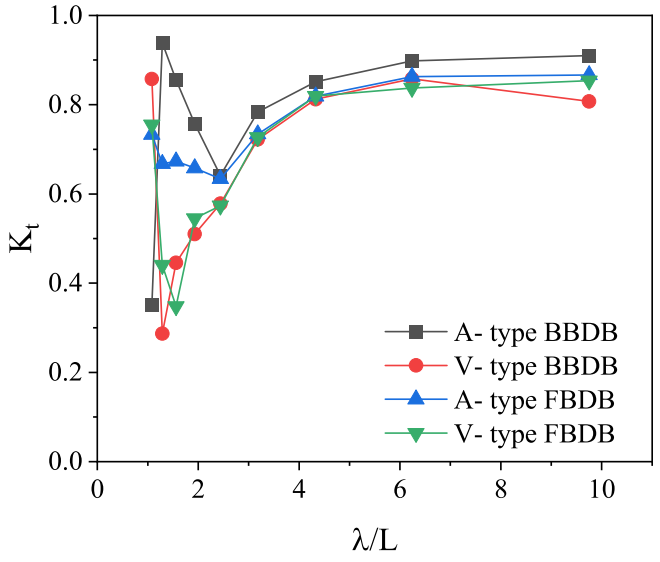

Fig. 9. Variation of K_t with λ/L under four different configurations.

The observed differences in CWR are primarily driven by changes in wave incidence direction, with the shape of the buoyancy chamber having a smaller impact.

4.2.2. Wave transmission coefficient performance

Fig. 9 presents a comparison of the K_t across four different configurations. A-type buoyancy chambers, whether BBDB or FBDB, exhibit a similar trend, with consistently higher K_t values. In contrast, V-type buoyancy chambers, both BBDB and FBDB, show comparable trends with relatively lower K_t. Between $\lambda/L = 1.08$ and $\lambda/L = 2.44$, the K_t drop sharply for the V-type buoyancy chamber configurations, whereas the A-type buoyancy chamber configurations maintain relatively higher values. This indicates that at smaller λ/L, the V-type buoyancy chambers outperform A-type buoyancy chambers by reducing the K_t more effectively. After $\lambda/L = 2.44$, as the wavelength ratio increases, all values converge, and differences between types diminish, showing similar performance trends. Additionally, V-type FBDB achieves the lowest average K_t of 0.642, followed by V-type BBDB at 0.653. In contrast, A-type FBDB and A-type BBDB maintain higher averages of 0.746 and 0.776, respectively. The shape of the buoyancy chamber (A-type or V-type) determines the overall performance, where V-type chambers achieve better results.

Figs. 8 and 9 suggest a correlation between the CWR peaks and the inflexion points of the K_t across the four model configurations, indicating a possible interplay between wave energy capture and wave attenuation mechanisms in WEC systems.

The V-type buoyancy chamber BBDB stands out for its superior overall performance, combining high wave energy capture efficiency with effective wave attenuation. Although the A-type buoyancy chamber BBDB-WEC also excels in energy capture, it performs less effectively in wave attenuation. However, given the priority of maximising energy capture, both the A-type and V-type buoyancy chamber BBDB-WEC have been selected for further analysis of baffle performance. The maximum value for the V-type and the minimum value for the A-type both occur at $\lambda/L = 1.08$, which may be attributed to the buoyancy chambers of the BBDB generating secondary waves. These secondary waves could introduce an additional dominant frequency, potentially leading to extreme values under certain conditions. However, this effect is distinct from structural resonance.

4.3. Effect of the addition of baffles

4.3.1. Effect on CWR

Fig. 10 shows the variation of CWR with λ/L for A-type buoyancy chamber BBDB-WEC with different baffle spacings. It indicates that increasing the spacing between baffles generally leads to a corresponding increase in the CWR for the A-type buoyancy chamber BBDB. However, the performance of the BBDB-WEC improves only when the baffle spacing exceeds 0.8 m; for spacing less than 0.8 m, the CWR drops compared to the configuration without baffles. As λ/L increases, the CWR rises between $\lambda/L = 1.08$ and $\lambda/L = 2.44$, but begins to decline after $\lambda/L = 2.44$. The performance improvement is most significant when the baffle spacing is 1 m. This increase is more pronounced in the range of $\lambda/L = 2.44$ to $\lambda/L = 9.75$ than in the range of $\lambda/L = 1.08$ to $\lambda/L = 2.44$. Notably, the maximum rise in CWR is observed at $\lambda/L = 2.44$, where it peaks at 126.35 %, thereby broadening the peak performance range of the BBDB-WEC. For the spacing 1 m configuration, the average CWR reaches a maximum of 57.06 %, which is 8.99 % higher than the value of without baffles configuration, which is 48.07 %.

Fig. 11 presents a comparison of CWR for the V-type buoyancy chamber BBDB-WEC with and without baffles, as well as at varying baffle spacings. The trend in CWR changes is like that of the A-type

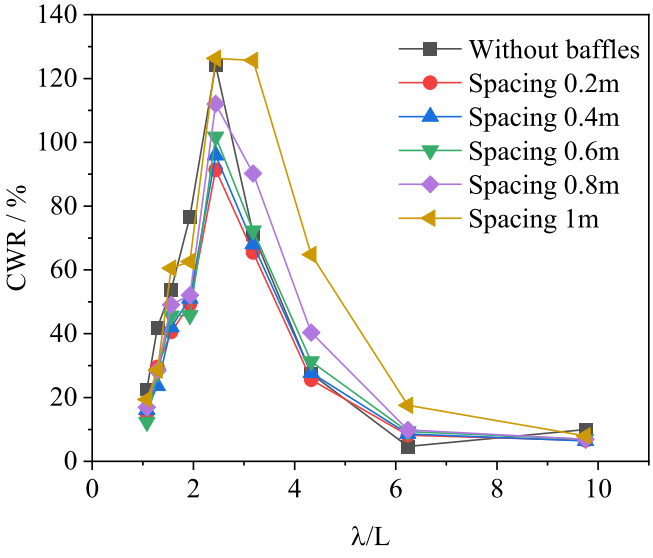

Fig. 10. Comparison of CWR for A-type buoyancy chamber BBDB-WEC with different baffle spacings.

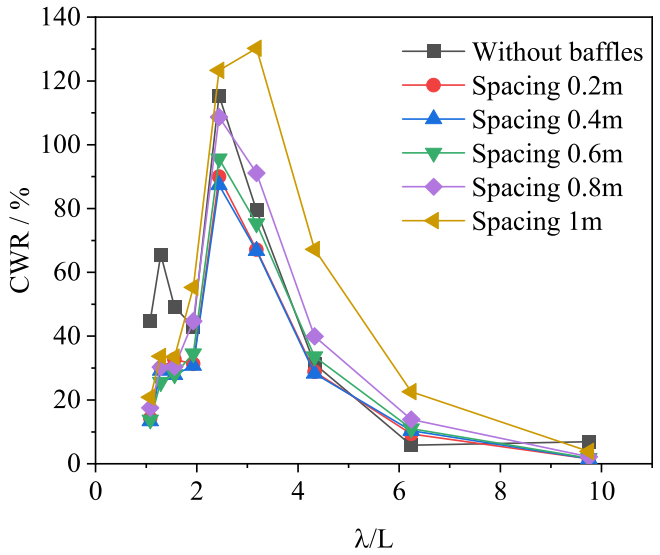

Fig. 11. Comparison of CWR for V-type buoyancy chamber BBDB-WEC with different baffle spacings.

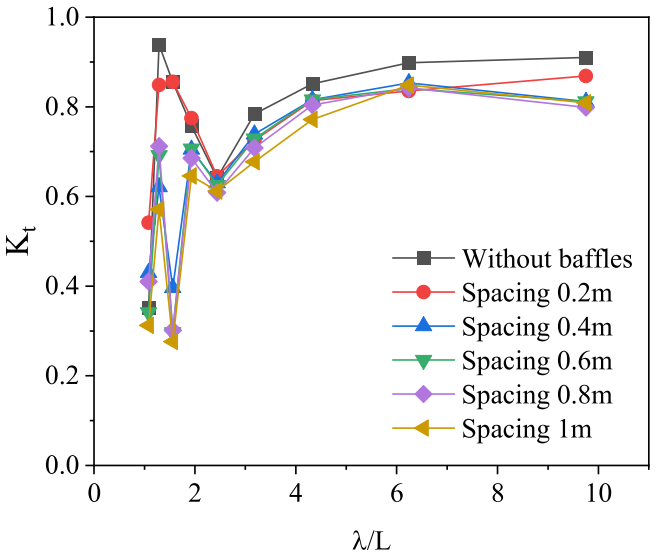

Fig. 12. Comparison of transmission coefficient in A-type buoyancy chamber BBDB-WEC with different baffle spacings.

buoyancy chamber BBDB-WEC, where the CWR increases as the spacing between the baffles increases. At a 1 m spacing, the model demonstrates the highest wave energy capture capability, reaching a peak CWR of 130.21 % at $\lambda/L = 3.18$, which is a 50.8 % improvement compared to the model without baffles. For the spacing 1 m configuration, the average CWR reaches a maximum of 54.49 %, which is 5.44 % higher than the value of without baffles configuration, which is 49.05 %.

The CWR comparison of A-type and V-type buoyancy chamber BBDB-WECs with 1 m baffles, as shown in Table 5. The A-type performs exceptionally well at intermediate λ/L values, such as $\lambda/L = 2.44$, achieving the highest CWR of 126.35 %, making it ideal for wave energy capture in this range. In contrast, the V-type demonstrates a more stable performance across the entire λ/L range, with notable advantages at higher λ/L values, such as a CWR of 22.59 % at $\lambda/L = 6.24$. The average CWR is 57.06 % for A-type and 54.49 % for V-type BBDB-WECs. Thus, the A-type buoyancy chamber BBDB-WEC with a baffle spacing of 1 m demonstrates the best wave energy capture capability. This contrasts with the scenario without baffles, where the V-type buoyancy chamber BBDB loses its advantage in wave energy capture at lower λ/L, which also results in the V-type having a lower average CWR compared to the A-type.

4.3.2. Effect on wave transmission coefficient

Fig. 12 illustrates the variations in the K_t. For the A-type buoyancy chamber BBDB-WEC, the K_t begins to decrease after the installation of baffles, and this decrease becomes more pronounced as the baffle spacing increases. The BBDB-WEC shows the best wave dissipation performance at a baffle spacing of 1 m. Between $\lambda/L = 1.08$ and $\lambda/L = 1.93$, the wave dissipation performance of the BBDB-WEC has improved significantly. While at the range of $\lambda/L = 3.18$ to $\lambda/L = 9.75$, K_t decrease relatively steadily, with a drop ranging between 0.05 and 0.1. The average K_t for the 1 m spacing configuration is 0.614, which is 0.162 lower than the average K_t of 0.776 for the configuration without baffles.

Fig. 13 presents a comparison of the K_t for the V-type buoyancy chamber BBDB-WEC with the A-type buoyancy chamber BBDB. The wave attenuation performance of the BBDB-WEC improves with the installation of baffles and increasing baffle spacing. The K_t increases overall with the λ/L. It fluctuates significantly in the short-wave range ($\lambda/L = 1.08 \sim 1.56$), grows steadily in the mid-wave range ($\lambda/L = 1.93 \sim 3.18$), and stabilises with a saturating trend in the long-wave range ($\lambda/L = 4.33 \sim 9.75$), demonstrating stronger adaptability. The average K_t for the 1 m spacing configuration is 0.575, which is 0.078 lower than the average K_t of 0.653 for the configuration without baffles.

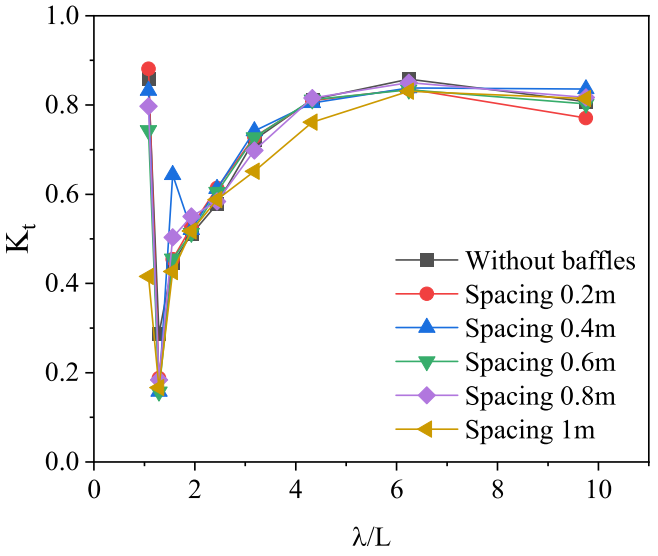

Fig. 13. Comparison of transmission coefficient in V-type buoyancy chamber BBDB-WEC with different baffle spacings.

In summary, the baffles effectively reduce K_t, with the 1 m spacing

Table 5
CWR Comparison of A-type and V-type buoyancy chamber BBDBs with 1 m baffles.

Configurations	λ/L								
	1.08	1.29	1.56	1.93	2.44	3.18	4.33	6.24	9.75
A-type buoyancy chamber BBDB-WEC	19.4	28.55	60.55	62.58	126.35	125.71	64.82	17.56	7.98
V-type buoyancy chamber BBDB-WEC	20.82	33.68	33.44	55.25	123.31	130.21	67.2	22.59	3.88

configuration showing the best performance. Table 6 compares the K_t values of A-type and V-type buoyancy chamber BBDBs with 1 m spacing. Table 6 compares the K_t values of A-type and V-type buoyancy chamber BBDBs with 1 m spacing. The A-type exhibits significant performance fluctuations in the short-wave range ($\lambda/L = 1.08 \sim 1.56$), while the V-type shows a more consistent performance. With an average K_t of 0.575, which is lower than that of the A-type at 0.614, the V-type demonstrates better wave attenuation performance.

4.3.3. Effect on mooring force

Figs. 14 and 15 show the mooring force for A-type and V-type buoyancy chamber BBDB-WECs, respectively. The mooring force for the A-type buoyancy chamber BBDB model remains unaffected by variations in baffle spacing, with no significant differences observed compared to the force for the model without baffles. The force magnitude is relatively consistent across different λ/L.

In contrast, the V-type buoyancy chamber BBDB-WEC shows that as the baffle spacing increases, the force variation becomes more complex. However, across most λ/L, the forces experienced by the model without baffles exceed those of the model with baffles, indicating that baffle installation in this buoyancy chamber design helps reduce the load on the mooring system.

Fig. 16 compares the mooring force of A-type and V-type buoyancy chamber BBDBs with 1 m baffles. The mooring force increases with the rise in λ/L, fluctuating slightly within the range of $\lambda/L = 1.08 \sim 3.18$ before reaching a peak. It then slowly decreases between $\lambda/L = 3.18$ and $\lambda/L = 6.24$, followed by another increase beyond $\lambda/L = 6.24$. While both shapes follow similar trends, the V-type consistently exerts lower forces on the mooring system than the A-type, with a reduction of approximately 1 N across all frequency ranges.

The load on the A-type buoyancy chamber did not show significant variation with increased spacing, while the mooring force on the configuration V-type buoyancy chamber exhibited more dispersion. This dispersion in load could be attributed to the V-shaped region, which tends to focus and concentrate wave energy, leading to localised impacts on the model. The combined effect of this impact force and the different baffle spacings causes the load values to vary across various λ/L. Since this impact force is directed opposite to the direction of the incoming waves, the forces on the mooring system for the V-type float counteract each other, resulting in the mooring force acting on the V-type always being smaller than that on the A-type. The V-type WEC shows a larger impact. This is likely due to the streamline shape of the A-type, while the V-type has a complex interaction with flows and is more sensitive to the baffle change.

4.3.4. Effect on WEC motion

The pitch motion of the A-type and V-type buoyancy chamber BBDB-WECs is depicted in Fig. 17. The RAO_{Pitch} gradually increases with the increase of λ/L. When the baffle spacing is 1 m, the RAO is generally lower than that of other spacings. Fig. 18 compares the heave motion of the A-type and V-type buoyancy chamber BBDB-WECs. Both designs exhibit a similar trend in heave motion, with a general increase as λ/L increase. When comparing the heave motion of the A-type and V-type, there is no significant difference between the two curves. The surge motion of the A-type and V-type buoyancy chamber BBDB-WECs is depicted in Fig. 19. The RAO_{surge} gradually increases with the increase of λ/L. The RAO_{surge} decreases as the spacing increases.

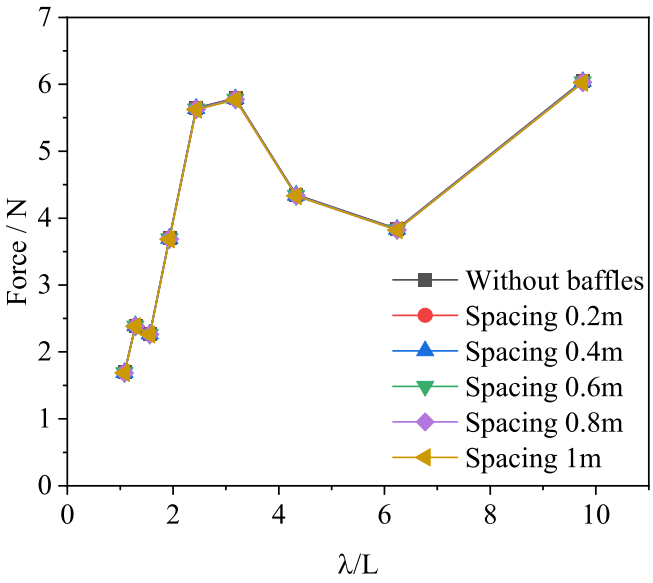

Fig. 14. Comparison of mooring force for A-type buoyancy chamber BBDB-WEC with different baffle spacings.

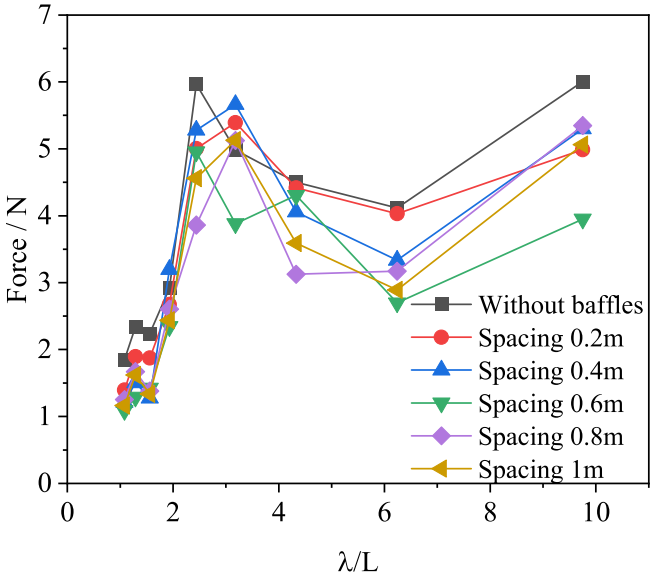

Fig. 15. Comparison of mooring force for V-type buoyancy chamber BBDB-WEC with different baffle spacings.

With the increase of λ/L, RAO_{Pitch}, RAO_{Heave}, and RAO_{Surge} gradually increase. Increasing the baffle spacing generally helps reduce the motion of the model, particularly the pitch motion and surge motion. There is a correlation between pitch motion and CWR. Specifically, when combining Figs. 17–19, it indicates that as the RAO_{Pitch} of configurations with a 1 m spacing decrease relative to that of configurations without baffles, the CWR increases, and vice versa. The elasticity of the mooring system may contribute to the RAO approaching 1.0 at certain

Table 6
Transmission coefficient comparison of A-type and V-type buoyancy chamber BBDBs with 1 m baffles.

Configurations	λ/L								
	1.08	1.29	1.56	1.93	2.44	3.18	4.33	6.24	9.75
A-type buoyancy chamber BBDB-WEC	0.312	0.571	0.276	0.646	0.612	0.678	0.772	0.849	0.809
V-type buoyancy chamber BBDB-WEC	0.416	0.167	0.427	0.518	0.588	0.651	0.761	0.831	0.815

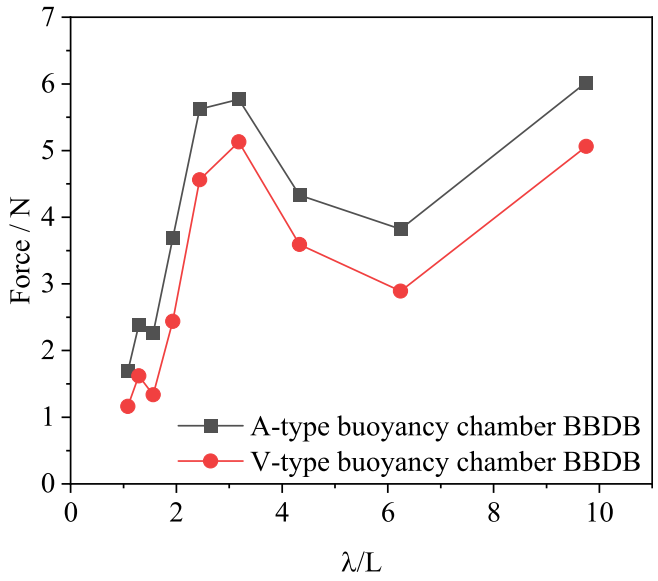

Fig. 16. Comparison of mooring force for A-type and V-type buoyancy chamber BBDBs with 1 m baffles.

frequencies.

5. Conclusions

In this study, by comparing and analysing existing WEC and breakwater structures and theories, a new structure has been developed, combining OWC-WEC technology with a catamaran-style breakwater (BDB-WEC with baffles). This structure was designed to serve as a breakwater for floating solar farms. Additionally, two different buoyancy chamber shapes (A-type and V-type) were designed for the model.

The performance of the model and the effectiveness of the baffles were tested within the $\lambda/L = 1.08 \sim 9.75$. The analysis focused primarily on CWR and wave transmission coefficient to evaluate the model's energy capture and wave attenuation capabilities. Additionally, the study examined the loads on the mooring system, the motion patterns of the model, and the relationships between these parameters. To achieve these objectives, the experiment utilised a total of 9 sensors: 4 Wave gauges, 2 pressure sensors, 2 force sensors, and one accelerometer-inclinometer, and collected data from 153 cases.

After the experiment, the optimal nozzle ratio was 1.03 %, with BBDB outperforming FBDB. The performance of the A-type and V-type buoyancy chambers were relatively close, with each showing distinct advantages under higher λ/L. Baffles can effectively enhance the energy capture capability of the OWC-WEC, particularly when the wavelength of the waves is relatively long. In ocean environments, long waves are

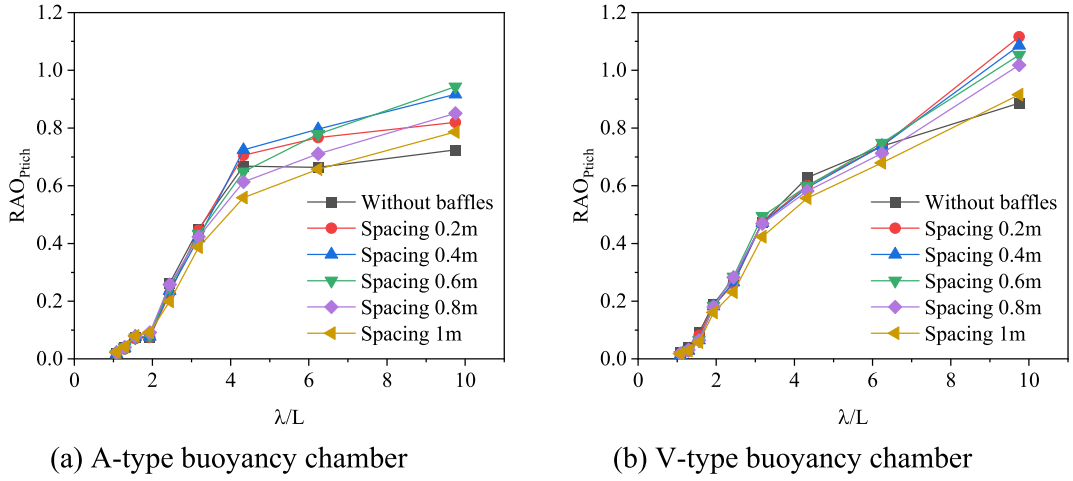

Fig. 17. Comparison of pitch motion in BBDB-WEC with different baffle spacings.

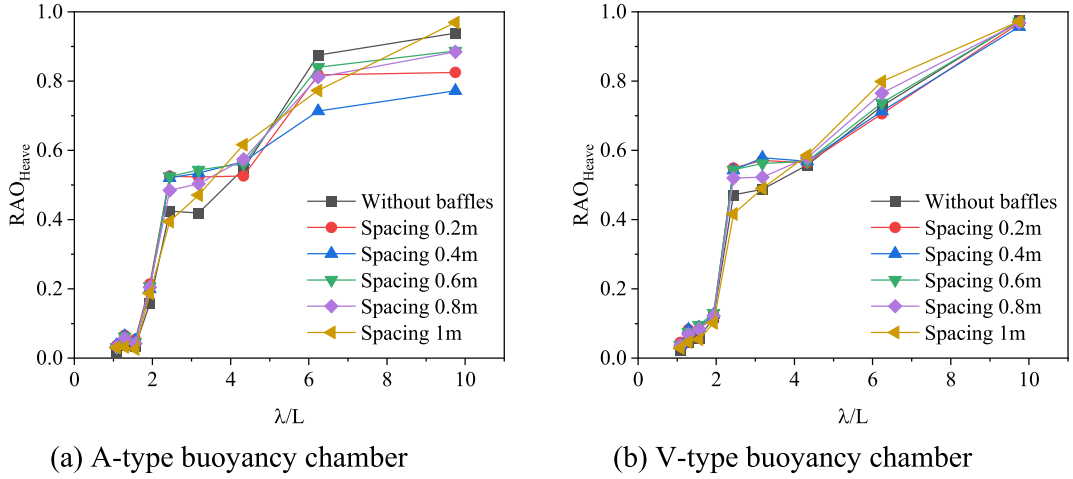

Fig. 18. Comparison of heave motion in BBDB-WEC with different baffle spacings.

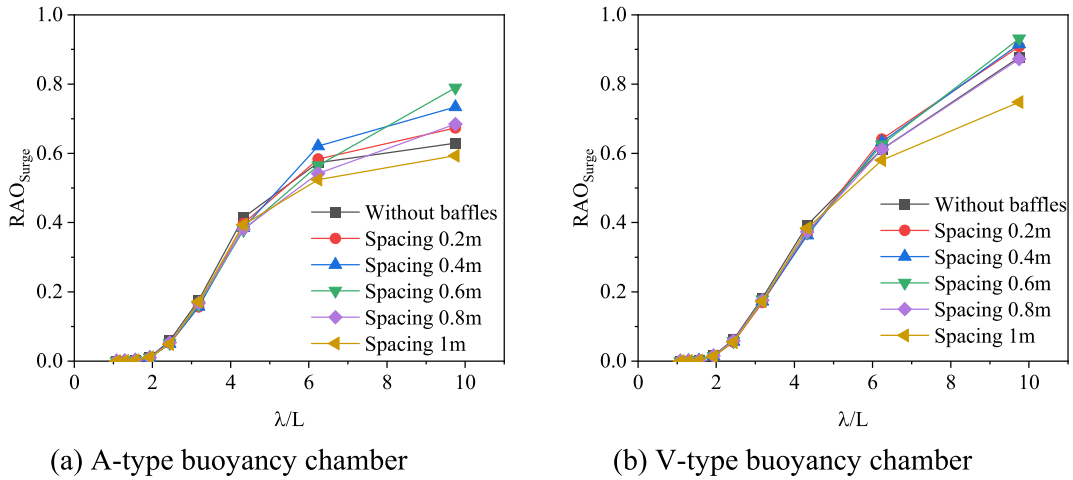

Fig. 19. Comparison of surge motion in BBDB-WEC with different baffle spacings.

more common, highlighting the significant practical value of baffles. Moreover, baffles can reduce the transmission coefficient, especially when it experiences an abnormal increase at specific wavelengths, demonstrating excellent wave attenuation performance. Baffles can also reduce heave and pitch motion, indicating that minimising movement in these two degrees of freedom can improve BBDB-WEC performance.

The V-type buoyancy chamber slightly outperformed the A-type, improving energy capture and wave dissipation while reducing the load on the mooring lines. Therefore, the optimal model configuration is a V-type buoyancy chamber BBDB-WEC with baffles spacing of 1 m. Additionally, its creation of two oscillating water column regions enables integration with other WECs, such as oscillating bodies, to further improve energy capture efficiency—a promising direction for future research.

The two anomalies observed during the experiment, namely the significant drop in the Transmission Coefficient for the A-type buoyancy chamber BBDB at $\lambda/L = 1.54$ and the sharp decline in the CWR for the V-type buoyancy chamber BBDB between $\lambda/L = 1.54$ and $\lambda/L = 1.08$, could serve as focal points for future research. Investigating the causes of these anomalies could provide deeper insights into the OWC-WEC system and help optimise the structure. Additionally, installing an air turbine on the model would allow for assessing the structure's final power generation capacity.

Data availability

All data underlying the results are available as part of the article and no additional source data are required.

CRediT authorship contribution statement

Xiangcheng Lyu: Writing – review & editing, Writing – original draft, Validation, Methodology, Investigation, Formal analysis, Conceptualization. **Chenhao Mi:** Methodology, Investigation. **Stan Collions:** Methodology, Investigation. **Wenchuang Chen:** Writing – review & editing, Supervision, Methodology, Investigation. **Danlei Yang:** Writing – review & editing, Supervision, Investigation. **Luofeng Huang:** Writing – review & editing, Supervision, Methodology, Investigation, Funding acquisition.

Declaration of competing interest

The authors declare that they have no known competing financial interests or personal relationships that could have influenced the work reported in this paper.

Acknowledgements

L.H. acknowledges grants received from Innovate UK (No. 10048187, 10079774, 10081314), the Royal Society (IEC\NSFC\223253, RG\R2\232462) and UK Department for Transport (TRIG2023 – No. 30066).

References

Adibzade, M., Akbari, H., 2023. Spectral approach to evaluate multi-body floating wave energy converters in complex sea states. Ocean Eng. 286. https://doi.org/10.1016/j.oceaneng.2023.115567.

Adibzade, M., Akbari, H., 2024. Fully spectral approach to evaluate the performance of floating wave energy converters in directional complex sea states. Ocean Eng. 306. https://doi.org/10.1016/j.oceaneng.2024.117999.

Cebada-Relea, A., López, M., Aenlle, M.L., 2022. Time-domain numerical modelling of the connector forces in a modular pontoon floating breakwater under regular and irregular oblique waves. Ocean Eng. 243, 110263. https://doi.org/10.1016/j.oceaneng.2021.110263.

Chen, T., Wu, B., Li, M., 2017. Flume experiment study on capture width ratio of a new backward bent duct buoy with a pentagon buoyancy cabin. Ocean Eng. 141, 12–17. https://doi.org/10.1016/j.oceaneng.2017.06.013.

Chen, W.C., Zhang, Y.L., Yang, J., Yu, H.F., Liang, S.D., 2021. Experiments and CFD modeling of a dual-raft wave energy dissipator. Ocean Eng. 237. https://doi.org/10.1016/j.oceaneng.2021.109648.

Chen, W., Huang, Z., Zhang, Y., Wang, L., Huang, L., 2024a. Hydrodynamic performance of a three-unit heave wave energy converter array under different arrangement. Renew. Energy 221. https://doi.org/10.1016/j.renene.2023.119808.

Chen, W., Xie, W., Zhang, Y., Wang, C., Wang, L., Huang, L., 2024b. Improving wave energy conversion performance of a floating BBDB-OWC system by using dual chambers and a novel enhancement plate. Energy Convers. Manag. 307. https://doi.org/10.1016/j.enconman.2024.118332.

Cheng, Y., Fu, L., Dai, S., Collu, M., Cui, L., Yuan, Z., Incecik, A., 2022. Experimental and numerical analysis of a hybrid WEC-breakwater system combining an oscillating water column and an oscillating buoy. Renew. Sustain. Energy Rev. 169. https://doi.org/10.1016/j.rser.2022.112909.

de, O., Falcão, A.F., 2010. Wave energy utilisation: a review of the technologies. Renew. Sustain. Energy Rev. 14 (3), 899–918. https://doi.org/10.1016/j.rser.2009.11.003. Author1, A.B. (University, City, State, Country); Author 2, C. (Institute, City, State, Country). Personal communication, 2012.

Delmonte, N., Barater, D., Giuliani, F., Cova, P., Buticchi, G., 2016. Review of oscillating water column converters. In: IEEE Transactions on Industry Applications, vol. 52. Institute of Electrical and Electronics Engineers Inc, pp. 1698–1710. https://doi.org/10.1109/TIA.2015.2490629, 2.

Endre Süli, David Francis Mayers, 2003a. An Introduction to Numerical Analysis. Cambridge University Press, 0-521-00794-1.

Endre Süli, David Francis Mayers, 2003b. An Introduction to Numerical Analysis. Cambridge University Press, 0-521-00794-1.

Göteman, M., 2017. Wave energy parks with point absorbers of different dimensions. J. Fluid Struct. 74, 142–157. https://doi.org/10.1016/j.jfluidstructs.2017.07.012.

He, F., Huang, Z., 2014. Hydrodynamic performance of pile-supported OWC-type structures as breakwaters: an experimental study. Ocean Eng. 88, 618–626. https://doi.org/10.1016/j.oceaneng.2014.04.023.

He, F., Huang, Z., 2017. Characteristics of orifices for modeling nonlinear power take-off in wave-flume tests of oscillating water column devices. J. Zhejiang Univ. - Sci. 18 (5), 329–345. https://doi.org/10.1631/jzus.A1600769.

Howe, D., Nader, J.R., 2017. OWC WEC integrated within a breakwater versus isolated: experimental and numerical theoretical study. Int. J. Mar. Energy 20, 165–182. https://doi.org/10.1016/j.ijome.2017.07.008.
Huang, L., Thomas, G., 2019. Simulation of wave interaction with a circular ice floe. J. Offshore Mech. Arctic Eng. 141, 041302.
IRENA, 2020. Innovation outlook: ocean energy technologies. Int. Renew. Energy Agency. 2020, 1–84.
IRENA, 2023a. Ocean energy technologies A brief from the IRENA collaborative framework on ocean energy and offshore renewables. www.irena.org.
IRENA, 2023b. Ocean energy technologies A brief from the IRENA collaborative framework on ocean energy and offshore renewables. www.irena.org.
Khurshid, H., Mohammed, B.S., Al-Yacouby, A.M., Liew, M.S., Zawawi, N.A.W.A., 2024. Analysis of hybrid offshore renewable energy sources for power generation: a literature review of hybrid solar, wind, and waves energy systems. Develop. Built Environ. 19, 100497. https://doi.org/10.1016/j.dibe.2024.100497.
Kisacik, D., Stratigaki, V., Wu, M., Cappietti, L., Simonetti, I., Troch, P., Crespo, A., Altomare, C., Domínguez, J., Hall, M., Gómez-Gesteira, M., Canelas, R.B., Stansby, P., 2020a. Efficiency and survivability of a floating oscillating water column wave energy converter moored to the seabed: an overview of the EsflOWC MaRINET2 Database. Water (Switzerland) 12 (4). https://doi.org/10.3390/W12040992.
Kisacik, D., Stratigaki, V., Wu, M., Cappietti, L., Simonetti, I., Troch, P., Crespo, A., Altomare, C., Domínguez, J., Hall, M., Gómez-Gesteira, M., Canelas, R.B., Stansby, P., 2020b. Efficiency and survivability of a floating oscillating water column wave energy converter moored to the seabed: an overview of the EsflOWC MaRINET2 Database. Water (Switzerland) 12 (4). https://doi.org/10.3390/W12040992.
Koo, W., 2009. Nonlinear time–domain analysis of motion-restrained pneumatic floating breakwater. Ocean Eng. 36 (9–10), 723–731. https://doi.org/10.1016/J.OCEANENG.2009.04.001.
Li, M., Wu, B. jun, Jiang, C. you, Zhang, Y. qiu, 2019. Effect of reciprocating and unidirectional airflow on primary conversion of a pentagonal Backward Bent Duct Buoy. Appl. Ocean Res. 89, 85–95. https://doi.org/10.1016/j.apor.2019.05.010.
Mani, J., 1991. Design of Y-frame floating breakwater. J. Waterw. Port, Coast. Ocean Eng. 117 (2), 105–119. https://doi.org/10.1061/(ASCE)0733-950X(1991)117:2(105)452.
Mao, P., Chen, C., Chen, X., Zhang, Q., Bao, Y., Yang, Q., 2024. An innovative design for floating breakwater with Multi-objective genetic optimal method. Ocean Eng. 312, 119202. https://doi.org/10.1016/j.oceaneng.2024.119202.
Masuda, Y., Mccormick, M.E., 1987. Experiences in pneumatic wave energy conversion in Japan. https://api.semanticscholar.org/CorpusID:113787587.
McCartney, B.L., 1985. Floating breakwater design. J. Waterway Port Coast. Ocean Eng. Asce 111, 304–318. https://api.semanticscholar.org/CorpusID:110251199.
Mia, M.R., Zhao, M., Wu, H., Dhamelia, V., Hu, P., 2022. Hydrodynamic performance of a floating offshore oscillating water column wave energy converter. J. Mar. Sci. Eng. 10 (10). https://doi.org/10.3390/jmse10101551.
Mustapa, M.A., Yaakob, O.B., Ahmed, Y.M., Rheem, C.K., Koh, K.K., Adnan, F.A., 2017. Wave energy device and breakwater integration: a review. In: Renewable and Sustainable Energy Reviews, vol. 77. Elsevier Ltd, pp. 43–58. https://doi.org/10.1016/j.rser.2017.03.110.
Ning, D., Zhao, X., Göteman, M., Kang, H., 2016. Hydrodynamic performance of a pile-restrained WEC-type floating breakwater: an experimental study. Renew. Energy 95, 531–541. https://doi.org/10.1016/j.renene.2016.04.057.
Pecher, A., Kofoed, J.P., 2017. Handbook of Ocean Wave Energy. Springer International Publishing.
Qiao, D., Haider, R., Yan, J., Ning, D., Li, B., 2020. Review of wave energy converter and design of mooring system. In: Sustainability (Switzerland), vol. 12. MDPI. https://doi.org/10.3390/su12198251, 19.
Sheng, W., Flannery, B., Lewis, A., Alcorn, R., 2012. Experimental studies of a floating cylindrical OWC WEC. In: http://asmedigitalcollection.asme.org/OMAE/proceedings-pdf/OMAE2012/44946/169/4429015/169_1.pdf.
Solomin, E., Sirotkin, E., Cuce, E., Selvanathan, S.P., Kumarasamy, S., 2021. Hybrid floating solar plant designs: a review. Energies 14 (10). https://doi.org/10.3390/en14102751. MDPI AG.
Sundar, V., 2010. Conceptual design OF OWC wave energy converters combined with breakwater structures. In: http://asmedigitalcollection.asme.org/OMAE/proceedings-pdf/OMAE2010/49118/479/4587794/479_1.pdf.
Toyota, K., Nagata, S., Imai, Y., Setoguchi, T., 2008. Effects of hull shape on primary conversion characteristics of a floating OWC "backward bent duct buoy.". J. Fluid Sci. Technol. 3 (3), 458–465. https://doi.org/10.1299/jfst.3.458.
Tumse, S., Bilgili, M., Yildirim, A., Sahin, B., 2024. Comparative analysis of global onshore and offshore wind energy characteristics and potentials. Sustainability 16 (15). https://doi.org/10.3390/su16156614.
Uddin, Md J., Mir, Md Moheuddin, Kowsher, Md, 2019. A new study of trapezoidal, simpson's 1/3 and simpson's 3/8 rules of numerical integral problems. Appl. Math. Sci. Int. J. 6 (4), 1–13. https://doi.org/10.5121/mathsj.2019.640.
Vryhof Anchors, B.V., 2015. In: Vryhof Manual the Guide to Anchoring, fifth ed., vol. 49, pp. 25–41 1–2.
Wang, C., Zhang, Y., Xu, H., Chen, W., 2024. Wave power extraction from an integrated system composed of a three-unit oscillating water column array and an inclined breakwater. Renew. Sustain. Energy Rev. 202. https://doi.org/10.1016/j.rser.2024.114645.
Wehausen, John V., Laitone, E.V., 1960. Surface waves. In: Truesdell, C. (Ed.), Fluid Dynamics/Strömungsmechanik. Springer Berlin Heidelberg, pp. 446–778. https://doi.org/10.1007/978-3-642-45944-3_6.
Widagdo, A.B., Sujoko, S.U., Subarkah, A., Aziiz, S.A., Sukmana, C.I., Saputra, A.D., 2020. Study of wave deformation around floating breakwater. J. Phys. Conf. Ser. 1625 (1), 012055. https://doi.org/10.1088/1742-6596/1625/1/012055.
Windt, C., Davidson, J., Ringwood, J.V., 2021. Numerical analysis of the hydrodynamic scaling effects for the Wavestar wave energy converter. J. Fluid Struct. 105. https://doi.org/10.1016/j.jfluidstructs.2021.103328.
Wu, B., Li, M., Wu, R., Zhang, Y., Peng, W., 2017. Experimental study on primary efficiency of a new pentagonal backward bent duct buoy and assessment of prototypes. Renew. Energy 113, 774–783. https://doi.org/10.1016/j.renene.2017.06.010.
Zhang, C., Dai, J., Cui, L., Ning, D., 2023. Experimental study of nonlinear states of oscillating water column in waves. Phys. Fluids 35 (1). https://doi.org/10.1063/5.0129191.
Zhao, X.L., Ning, D.Z., Liang, D.F., 2019. Experimental investigation on hydrodynamic performance of a breakwater-integrated WEC system. Ocean Eng. 171, 25–32. https://doi.org/10.1016/j.oceaneng.2018.10.036.
Zhu, W., Du, Z., Tu, Y., Huang, Y., Liang, B., Chen, X., Cao, G., Xiao, S., Yang, S., 2024. Experimental study of a backward bent duct buoy wave energy converter: effects of the air chamber and center of gravity height. Ocean Eng. 313. https://doi.org/10.1016/j.oceaneng.2024.119447.